Journal of Applied Physics ARTICLE scitation.org/journal/jap

Phase-field modeling of helium bubble evolution in nickel-graphene nanocomposite

Cite as: J. Appl. Phys. **125**, 215304 (2019); doi: 10.1063/1.5084238
Submitted: 5 December 2018 · Accepted: 13 May 2019 ·
Published Online: 4 June 2019

View Online Export Citation CrossMark

Guojia Ge,[1] Feida Chen,[1,2] Xiaobin Tang,[1,2,a)] Hai Huang,[1] Xiangyu Sun,[1] and Lulu Ji[1]

AFFILIATIONS

[1]Department of Nuclear Science and Technology, Nanjing University of Aeronautics and Astronautics, Nanjing 211106, China
[2]Jiangsu Engineering Laboratory of Nuclear Energy Equipment Materials, Nanjing 211106, China

[a)]**Author to whom correspondence should be addressed:** tangxiaobin@nuaa.edu.cn. **Tel.:** +86 13601582233.
Fax: +86 025 52112908-80407.

ABSTRACT

Metal–graphene (Gr) nanocomposites are regarded as potential anti-irradiation advanced materials for Gen-IV nuclear reactors. In this work, a phase-field model was proposed to simulate helium (He) bubble evolution of nickel–Gr (Ni/Gr) nanocomposite during constant irradiation at 800 K. Ni/Gr nanocomposite presented an earlier onset time of He bubble nucleation but eventually formed bubbles with smaller size and lower density than those of pure Ni. The early He bubbles nucleated along Ni/Gr interfaces, while a He depletion zone formed nearby consequently, which confirmed that Ni/Gr interfaces inhibit He bubble growth. The effects of vacancies and He atoms on the He bubble growth rate were also quantitatively analyzed. The amount of irradiation-induced vacancies acted as an effective rate-controlling factor that determined the bubble growth rate with respect to the He atoms.

Published under license by AIP Publishing. https://doi.org/10.1063/1.5084238

I. INTRODUCTION

Since graphene (Gr) was first isolated in 2004, it has received wide attention due to its high mechanical properties, superior electrical and thermal conductivity, and large surface area.[1] Metal–Gr nanocomposites can be prepared by incorporating Gr nanoparticles into the metal matrix.[2] This treatment can not only significantly enhance the mechanical properties of the original metal matrix but also effectively improve the corrosion resistance and radiation tolerance of the material. Many research groups have proven this phenomenon. For example, Yang *et al.*[3] demonstrated that the interface in the Cu/Gr/Cu composite provides a strong sink in trapping defects and selecting sites for their recombination by *ab initio* calculations. Using molecular dynamics simulations, Gonzalez *et al.*[4] found that carbon nanotubes in the nickel (Ni) matrix act as nanochimneys, thereby allowing helium (He) atoms to escape the damaged zone and reduce bubble formation in the matrix. Kim *et al.*[5] revealed that ultrahigh-strength V–Gr nanolayers have excellent radiation tolerance on the basis of He^+ irradiation study. The ability of Gr to hinder crack propagation also suppresses failure. Therefore, metal–Gr nanocomposites are regarded as a new generation of advanced anti-irradiation materials for nuclear power with substantial potential for application.

Future Gen-IV nuclear reactors with good functionality and capability pose considerable challenges to structural materials because of their extreme operating conditions. Particularly in the molten salt reactor, demanding materials both can resist molten fluoride corrosion and adapt to high neutron doses at elevated temperatures.[6–8] Ni-based superalloy is the candidate material at present. However, the study of the irradiation effect found that Hastelloy also exhibits substantial high-temperature embrittlement during service.[9] At high temperatures, the diffusion of vacancies produced by neutron cascade collisions and the He atoms from (n, α) transmutation reaction is accelerated. They are easy to combine to form He bubbles and facilitate growth with constant absorbing point defects, thereby resulting in material swelling and embrittlement.[10] To enhance the radiation tolerance of Ni-based alloy further, researchers proposed the Ni/Gr nanocomposite. Huang *et al.*[11] performed He^+ irradiation experiments on Ni/Gr, which exhibits lesser crystal defects than its pure counterpart.

Further research is needed to simulate the evolution of He bubbles in Ni/Gr under irradiation conditions to clarify the experimentally observed phenomena. Given the limitation of space and time scale, molecular dynamics cannot reflect the

Published under license by AIP Publishing.

morphological evolution and overall distribution of bubbles well. Among the methods of mesoscopic simulation, rate theory, cluster dynamics, and kinetic Monte Carlo are commonly used, but these methods are still difficult to predict the complex microstructure evolution accurately; meanwhile, the cost of calculation is large.[12]

Since 2009, the phase-field method has been gradually applied to simulate the irradiation effects of materials. This method is beneficial because it enables the investigation of the microstructural evolution driven by the free energy minimization of the multiphase structures that interact via diffusion.[13] Implementing a large spatial and time scale simulation in a limited computation time is also possible. In simulating the irradiation effects, the phase-field method bridges from atomistic simulations to macroscale simulations of material behavior, through combining the kinetic and thermodynamic parameters of defects calculated by atomic simulation with the defect generation and absorption terms used in rate theory.[14] Hence, this method can accurately predict the evolution of the microstructure of the material under irradiation conditions. For example, Ahmed *et al.*[15] demonstrated that phase-field model predictions agree with grain growth classical theory in UO_2. Ma *et al.*[16] investigated the morphology of γ-hydride precipitation in Zr by using a phase-field kinetic model, and the results agree well with those of the TEM observations. Chang *et al.*[17] found that the magnitude of the applied tensile stress accelerated the void swelling in the austenitic stainless steel, which is consistent with former experimental observations.

In this work, we investigated the evolution of He bubbles in Ni/Gr by using the phase-field method by combining with the molecular dynamics calculation results and rate theory terms. Elevated temperature and different irradiation conditions were studied to understand the radiation tolerance of Ni/Gr.

II. THEORIES AND METHODS

A. Principle of the phase-field method

Instead of using atoms (molecular dynamics simulation), the phase-field method describes the microstructure of materials by one or several continuum variables, which are called field variables.[18] For example, in the void growth in materials, the concentrations of vacancies and interstitials were used as field variables to describe the distribution of voids in materials.[17] The field variables can be substituted into corresponding time-dependent kinetic equations, as shown in Eqs. (1) and (2). A series of time-varying variables can be obtained by solving the kinetic equations, thereby reflecting the microstructure evolution.

The phase-field simulations of He bubble growth in Ni/Gr were conducted based on three assumptions, as follows: (1) He bubbles comprise the combination of He atoms and vacancies and (2) the bubble and solid phases can be distinguished by continuously varying order parameters $\eta(x, y)$. When $\eta(x, y) \approx 0$, the phase state of the point is the solid phase. Meanwhile, when $\eta(x, y) \approx 1$, the phase state is the bubble phase.[18] (3) Given that the diffusion rate of the interstitial atoms is much larger than the vacancies, most of the atoms migrate to the surface and disappear or absorbed by other defects.[19] Therefore, the interstitial atoms were disregarded in this study.

On the basis of the assumptions above, we selected the vacancy concentration c_v, He atom concentration c_g, and order parameter η as the field variables to describe He bubble evolution. The temporal evolution and spatial distribution of the three variables were calculated using the corresponding kinetic equations:

$$\frac{\partial c_v}{\partial t} = \nabla\left(M_v \nabla \frac{1}{N}\frac{\delta F}{\delta c_v}\right) + \xi_v(r,\ t) + P_v(r,\ t) - S_v(r,\ t), \quad (1)$$

$$\frac{\partial c_g}{\partial t} = \nabla\left(M_g \nabla \frac{1}{N}\frac{\delta F}{\delta c_g}\right) + \xi_g(r,\ t) + P_g(r,\ t) - S_g(r,\ t), \quad (2)$$

$$\frac{\partial \eta}{\partial t} = -L\frac{\delta F}{\delta \eta} + \xi_\eta(r,\ t). \quad (3)$$

Equations (1) and (2) are the Cahn–Hilliard-type equations[20] modified by the inclusion of point defect source and sink terms, respectively. Meanwhile, Eq. (3) is an Allen–Cahn-type equation.[21] The first terms in the right-hand sides of Eqs. (1) and (2) capture chemical diffusion and are typically used in the phase-field models, in which M represents the defects mobility. These equations are as follows:

$$M_v = \frac{D_v c_v}{k_B T}, \quad (4)$$

$$M_g = \frac{D_g c_g}{k_B T}. \quad (5)$$

The terms added onto Eqs. (1) and (2) represented the various defect performances that exist in a material undergoing irradiation damage. First, the stochastic functions ξ represent thermal fluctuations that can be thought as terms that represent the trapping and release of mobile point defects by subcritical clusters within the matrix.[22]

The ongoing production of vacancies and gas atoms due to irradiation was incorporated into the model via the source terms P. They are simply described as a linear function of vacancy concentration $P_i = P_i^0(1 - c_v)$, $(i = \text{vac},\ \text{gas})$, so that the production of vacancies and gas atoms is zero in bubbles. The main source of vacancies was the displacement damage caused by the neutron cascade collisions, and He atoms came from the (n, α) transmutation reaction. Therefore, the P_v^0 and P_g^0 values represent the degree of displacement damage and the rate of transmutation reaction caused by irradiation, respectively. In this study, we assume that an atomic displacement has a 20% probability of generating a vacancy. The final terms S were the defect sink terms, which are defined as follows:

$$S_v = S_v^{\text{Int}}(1 - \varphi)c_v, \quad (6)$$

$$S_g = S_g^{\text{Int}}(1 - \varphi)c_g, \quad (7)$$

where the parameter S_i^{Int} describes the annihilation efficiency of defects that can vary for different interface types. The parameter φ

Published under license by AIP Publishing.

was used to spatially distinguish matrix regions ($\varphi = 1$) from the interface regions ($\varphi < 1$),[23] and is defined as $\varphi = \sum_{i=1}^{p} \varphi_i^2$, where ϕ_i are order parameters representing unique grain orientations. The main driving force of the microstructure evolution was the minimization of the multiphase structures' free energy F. The function of F with respect to the field variables is defined as follows:

$$F = N \int [\, h(\eta) f^{\text{solid}}(c) + j(\eta) f^{\text{bubble}}(c) + f^{\text{grad}}(c,\ \eta)]\ dV. \quad (8)$$

The multiphase structure consists of three parts of free energy, namely, bulk solid, bubble, and gradient energies that were expressed c_v, c_g, and η, respectively. η can distinguish the bubble regions from the solid regions. Thus, the expression of η can be used to differentiate solid and bubble phases' contribution to the total free energy of the system, that is, in the bubble phase, if $\eta = 1$ and $h(\eta) = (\eta - 1)^2 = 0$, then the contribution of the solid energy is 0. Similarly, in the solid phase, if $\eta = 0$ and $j(\eta) = \eta^2 = 0$, then the contribution of the bubble energy is also 0. The three types of free energy are specifically defined as follows:

$$f^{\text{solid}} = E_v^f c_v + E_g^f c_g + k_B T[c_v \ln(c_v) + c_g \ln(c_g) + (1 - c_v - c_g)\ln(1 - c_v - c_g)], \quad (9)$$

$$f^{\text{bubble}} = (c_v - 1)^2 + [\mu_g^0 c_g + c_g k_B T \ln(c_g) + c_g k_B T \ln(k_B T)], \quad (10)$$

$$f^{\text{grad}} = \sum \frac{\kappa_\psi}{2} |\nabla \psi|^2, \quad \psi = c_v,\ c_g,\ \eta. \quad (11)$$

The free energy of the solid and bubble phases was mainly generated by the concentration of their heterogeneous constituents, where E^f is the formation energy of the defect, and μ_g^0 is the reference chemical potential of the gas atoms in the gas phase. The gradient energy was generated by the difference in the concentration at the heterophase interface.

B. Phase-field model of Ni/Gr

According to a previous study,[24] the formation energies of defects E^f at Ni matrix and Ni/Gr interface are different, which will lead to the different morphological evolutions of defects from those in pure Ni. Therefore, we can simulate the heterogeneous material by setting different defect formation energies at the matrix and interface. We also endue the interface with the ability of annihilating defects; therefore, the parameter S_i^{Int} mainly accounts for the annihilation efficiency of vacancies and He atoms at the Ni/Gr interface, which is given in Table I as constant. The defect sink term only works on the Ni/Gr interface, and the value in the matrix is 0 ($\varphi = 1$). Four models were established, as shown in Fig. 1. Model A was pure Ni with a size of $128l^* \times 128l^*$, l^* is the characteristic length, and $l^* = 1$ nm. Model A was used to explore whether the variation trends of the three field variables are consistent. The simulation size of model B was $256l^* \times 256l^*$, and three Grs of different morphologies were incorporated to compare the radiation tolerance of Ni/Gr with pure Ni. Model C was a simplified Ni/Gr model, which incorporated only one Gr in the central region and a variety of irradiation conditions were set to explore the evolution regularity of He bubbles on the Ni/Gr interface. The width of the Ni/Gr interface is the same as the characteristic length. The Gr is

TABLE I. Material properties of Ni/Gr used in the simulations.

Physical parameter	Symbol	Value	Reference
Temperature	T	800 K	This work
Characteristic length	l^*	1 nm	This work
Vacancy diffusivity	D_v	5.69×10^{-10} m^2/s	19
He diffusivity	D_g	9.10×10^{-6} m^2/s	29
Vacancy formation energy in Ni	E_v^f	1.4 eV	24
He formation energy in Ni	E_g^f	4.5 eV	Unpublished result
Vacancy formation energy in the Ni/Gr interface	E_v^*	1.0 eV	24
He formation energy in the Ni/Gr interface	E_g^*	3.5 eV	Unpublished result
Vacancy annihilation efficiency	S_v^{Int}	0.05	This work
He annihilation efficiency	S_g^{Int}	0.01	This work
Gradient energy coefficients	$k_{v,g,h}$	1.15×10^{-7} J/m	This work

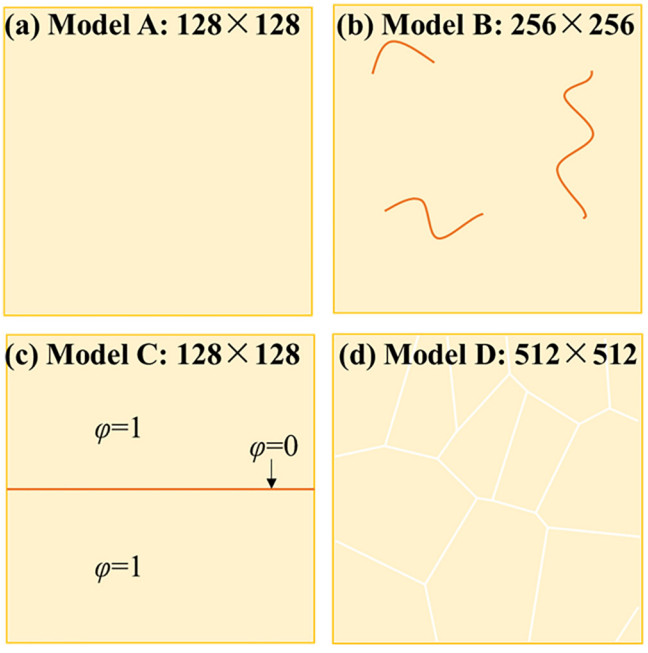

FIG. 1. Four phase-field models of pure Ni and Ni/Gr: (a) pure Ni, (b) Ni/Gr with three Gr, (c) Ni/Gr with one Gr, and (d) polycrystalline Ni.

Published under license by AIP Publishing.

included in the Ni/Gr interface because the width of Gr is so small compared to its interface. The Ni/Gr interface distinguishes from the matrix by setting different φ values as Model C shows. Model D was polycrystalline Ni with a size of $512l^* \times 512l^*$. In this model, the value of l^* was chosen as 10 nm and different grains had corresponding ϕ_i values.[25] Model D was used to investigate the role of different formation energy play in the evolution of He bubble.

In this work, we adopted the finite difference discretization to obtain the numerical solution of Eqs. (1)–(3). Solving equations in reduced from with nondimensionalized value. Thus, all parameters are normalized and can be derived as follows: length scale $\lambda = l/l^*$, time scale $\tau = t/t^*$ ($t^* = \lambda^2/D_v$), and energy scale $\varepsilon = E/k_BT$. The parameters used in the simulation are listed in Table I. The study on the He formation energy in the Ni and Ni/Gr interfaces has been previously conducted by our group. The gradient energy coefficients (κ) for vacancies, gas atoms, and η are assumed to be the same. The interfacial energy (γ) between Ni and He bubble can be numerically determined by κ following the approach of Cahn,[20] its derivation is given in the supplementary material. Throughout this paper, we use $\kappa_v = \kappa_g = \kappa_\eta = 1.15 \times 10^{-7}$ J/m, resulting in $\gamma = 2.48$ J/m^2, which is close to the value obtained from the previous study.[26–28]

III. RESULTS AND DISCUSSION

A. Bubble evolution in pure Ni and polycrystalline Ni

We first simulated the evolution of He bubbles in pure Ni (model A) and imaged the time-varying field variables obtained by solving the kinetic Eqs. (1)–(3). Figure 2 shows the change in c_v, c_g, and η at progressive instances in time during an irradiation simulation. With the continuous generation of vacancies and He atoms, He bubbles nucleated randomly in space and grow. In this process, the c_v value inside the bubbles was close to 1, and the c_g value was approximately 0.1. The change in η corresponded to the distribution and evolution of the He bubbles, which was consistent with c_v and c_g. These results confirmed that the simulated He bubble comprises vacancies and He atoms, and η can distinguish the bubble phase from the solid phase, which proved the accuracy of the phase-field model. In the follow-up simulations, we used η to reflect the evolution of the bubble.

In addition to monocrystalline Ni, we also investigated polycrystalline Ni. The source term of vacancy and He induced from irradiation remained the same as above. As shown in Fig. 3, bubbles were mainly formed at the grain boundary, which agreed with the experimental results. The slightly lower formation energy of defects at grain boundaries than that of matrix[30] in our work

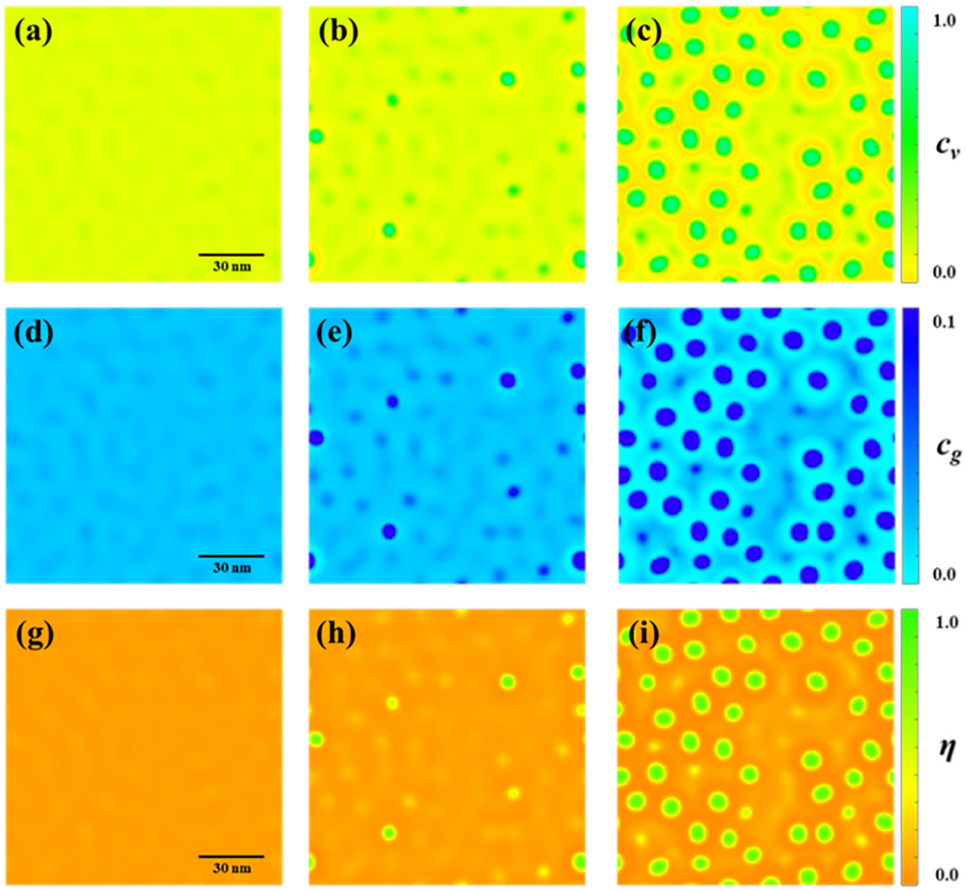

FIG. 2. Simulation snapshots of He bubble nucleation and growth in pure Ni. The top-to-bottom rows represent the contour plots of (a)–(c) vacancy concentration c_v, (d)–(f) He atom concentration c_g, and (g)–(i) order parameter η.

Published under license by AIP Publishing.

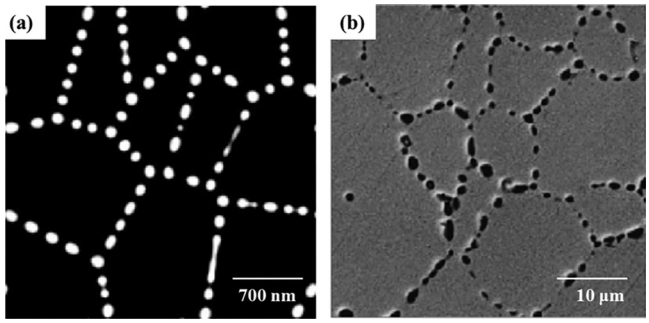

FIG. 3. (a) Simulation snapshot of the intergranular bubbles in polycrystalline Ni. (b) Microscopy image of the intergranular bubbles from a previous study.[31] Reproduced with permission from Zacharie *et al.*, J. Nucl. Mater. **255**, 85 (1998). Copyright 1998 Elsevier.

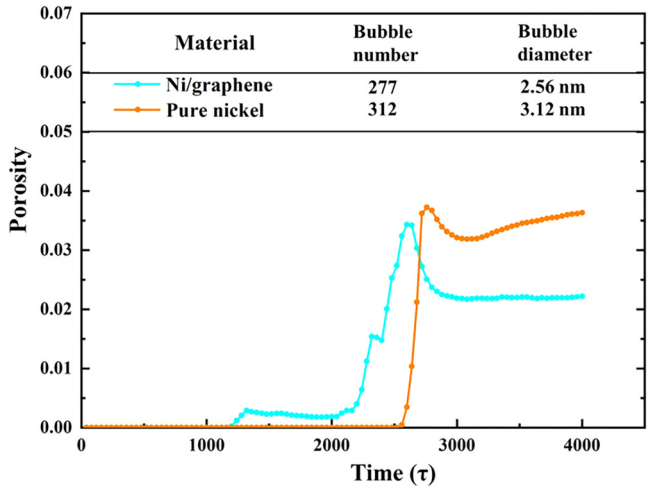

FIG. 4. Evolution of the porosity of Ni/Gr and pure Ni. The final number and mean size of bubbles are listed in the upper table.

played an important role in boundary segregation. Therefore, we believe that this characterization can also be used to describe the Ni/Gr interface if the accurate formation energy of defects is provided.

B. Comparison of Ni/Gr with pure Ni

After demonstrating the feasibility of the phase-field method in the He bubble growth simulation, we conducted a case study by comparing the radiation tolerance of Ni/Gr with pure Ni. As described above, a Ni/Gr model (model B) was constructed in the simulation. The irradiation condition was 1 dpa for displacement damage and 2 at. % for the total concentration of He atoms. The simulated duration was 4000 τ; thus, $P_v^0 = 5 \times 10^{-5}\tau^{-1}$ and $P_g^0 = 5 \times 10^{-6}\tau^{-1}$.

To compare He bubble evolution of Ni/Gr and pure Ni quantitatively, we calculated the porosity, final number, and mean size of bubbles via field variables, and the data are shown in Fig. 4. The nucleation time of bubbles in Ni/Gr was much earlier than that of pure Ni, and the final porosity and the number of He bubbles were less than those of pure Ni. The porosity of Ni/Gr slightly increased at 1100 τ, which indicated the formation of some small bubbles. According to a previous study,[28] nucleation time is the key factor affecting the final morphologies of bubbles. Those early formed bubbles began the absorption of vacancies and He atoms, thereby inhibiting the increase in the defect concentration of matrix, which resulted in lower final porosity and bubble number than those of pure Ni. Therefore, the early nucleation time is the origin of anti-irradiation properties of Ni/Gr. However, some questions, such as where the first nucleation occurs and why does the porosity decrease before stabilization, remain unanswered.

We imaged the time-varying field variable η to investigate the evolution of He bubbles, as shown in Fig. 5. Bubbles were preferentially nucleated at the Ni/Gr interface, where the formation energies of vacancies and He atoms are lower than those of matrix (Table I). With the continuous generation of irradiation-induced vacancies, the next round of nucleation started in the Ni matrix at approximately 2400 τ. Finally, bubbles formed in the entire irradiated bulk, but a depletion region of bubbles existed around the interface. This phenomenon was observed due to the defect absorption of preferentially formed bubbles at the Ni/Gr interface as mentioned above, thereby resulting in the extremely low concentrations of vacancies and He atoms nearby to be nucleated.

Some bubbles disappeared from 2600 τ to 2800 τ, as shown in Figs. 5(d) and 5(e). This finding corresponded exactly to the decrease in Ni/Gr porosity. He bubbles can grow through the Ostwald ripening mechanism, that is, bubbles can absorb vacancies and He atoms dissociated from the small bubbles nearby.[32] Therefore, the total porosity may present a decreasing trend at a stage due to the disappearance of small bubbles, but the size of the large bubbles does not rapidly change. A similar phenomenon occurs after the first nucleation of bubbles in pure nickel. But soon, its porosity began to rise again.

C. Bubble evolution under different irradiation conditions

To explore the regularity of bubble evolution and determine the role of interface further, we constructed a simplified Ni/Gr model (model C) with different irradiations. We varied two key parameters in this set of simulations. Three different P_g^0 values with the same P_v^0 were established to reflect the evolution of the bubble under different transmutation reaction rates, whereas three different P_v^0 values with the same P_g^0 were set to study the influence of the displacement damage of the materials.

As shown in Fig. 6, porosity was first calculated, and the variation trend was consistent with the bubble evolution presented in Fig. 5. The first slight increase in porosity corresponded to bubble nucleation at the Ni/Gr interface, and the subsequent increased corresponded to the nucleation and growth process in the Ni matrix. The higher the intensity of irradiation is, the higher the

Published under license by AIP Publishing.

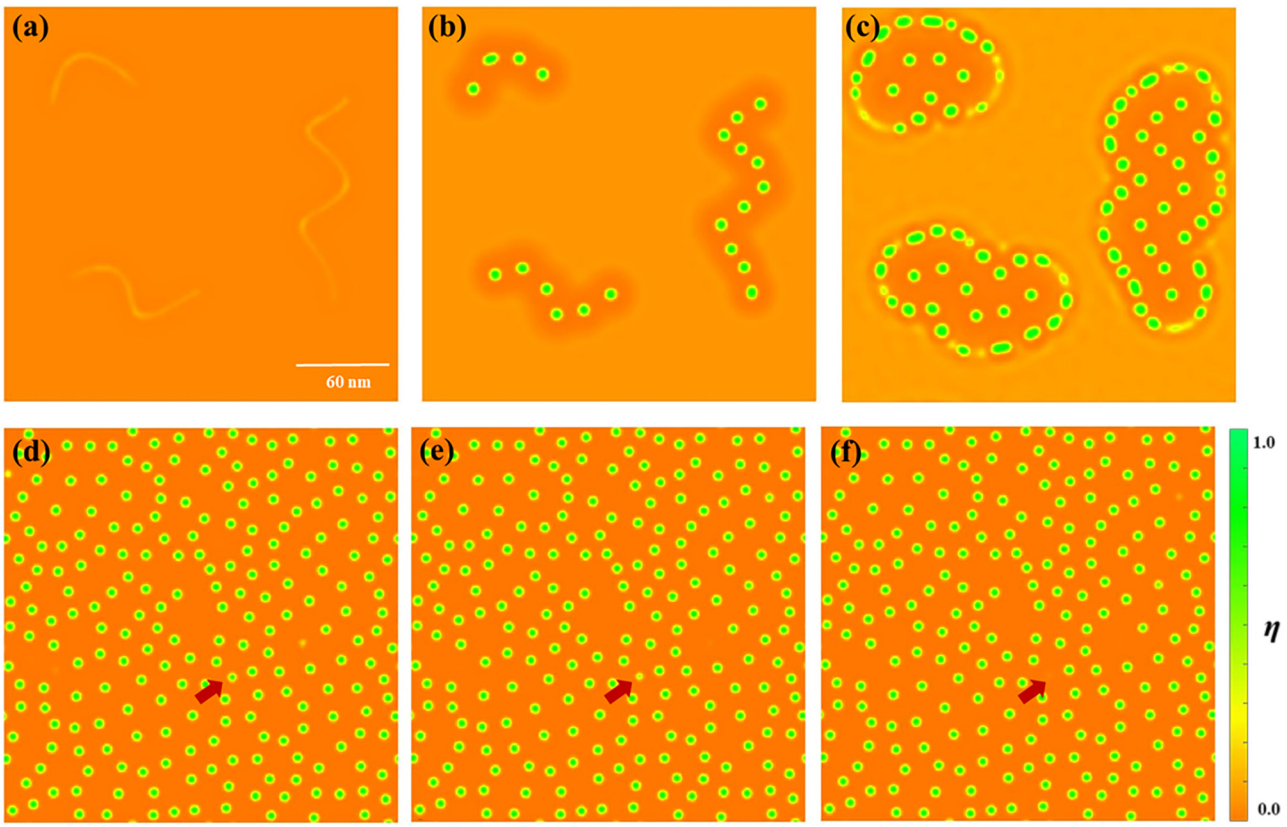

FIG. 5. Simulation snapshots of bubble nucleation and growth in Ni/Gr with three Gr. The simulation times are (a) 1000, (b) 2000, (c) 2400, (d) 2600, (e) 2700, and (f) 2800 τ. The red arrow points to the vanishing bubble.

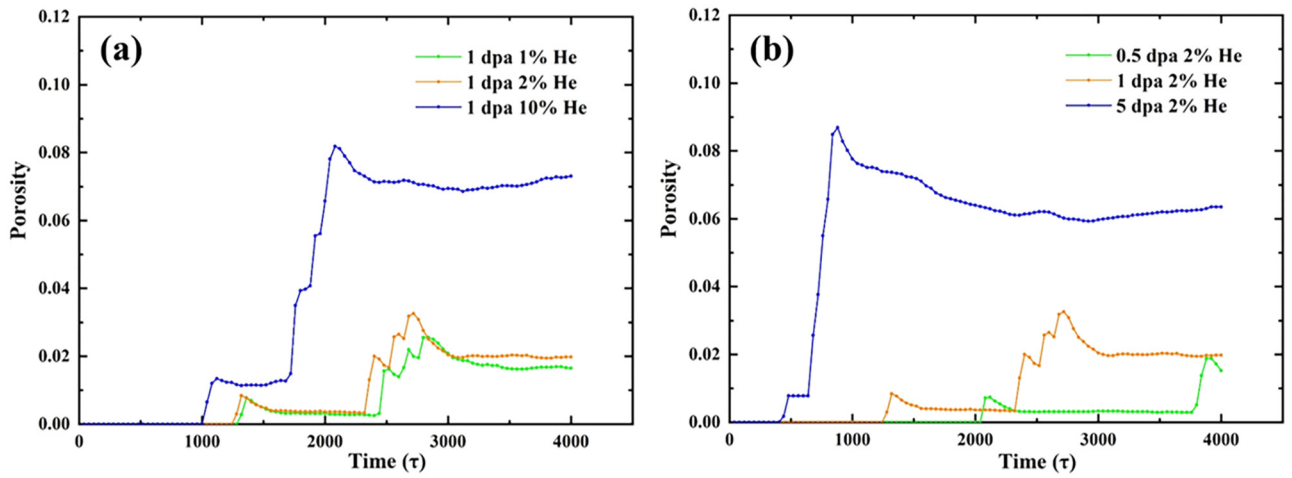

FIG. 6. Evolution of porosity in the presence of different (a) transmutation reaction rates and (b) degree of displacement damages.

Published under license by AIP Publishing.

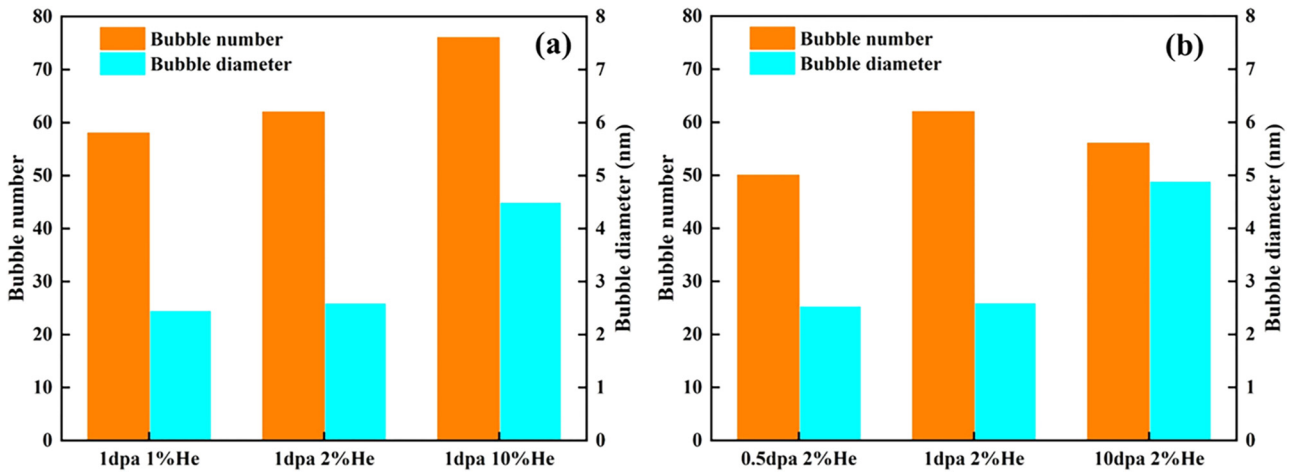

FIG. 7. Final number and mean size of He bubbles in the presence of different (a) transmutation reaction rates and (b) degree of displacement damages.

final stable porosity will be. Comparing Figs. 6(a) and 6(b) showed that the influence of the displacement damage on the bubble evolution was more evident than those of different transmutation reaction rates, which were mainly manifested by the difference in nucleation time. Thus, the change in material properties caused by displacement damage is significant. According to the bubble mechanics, the number of He atoms contained in a bubble of radius R can be described as $n_g = 8\pi\gamma R^2/3kT$, whereas the number of vacancies was $n_v = 4\pi R^3/3\Omega$. The n_g value increased as R^2 increased, but n_v increased with the increase in R^3. This phenomenon indicated that with the increase in the bubble radius R, much more vacancies were needed than the He atoms. Therefore, we can easily understand why vacancies act as an effective rate-controlling factor to determine the rate of bubble growth.

The final bubble number and mean size were calculated and shown in Fig. 7. As shown in Fig. 7(a), both numbers and sizes increased with the increase in He atom production rate when the displacement damage was constant. The generally accepted explanation for this phenomenon is that whether bubble can be nucleated is dominated by the fluctuation in free energy. We calculated the free energy at each grid by using Eqs. (8)–(11), and the results are shown in Fig. 8. A high c_g corresponded to high free energy, which indicated the considerable extent of system deviation from the equilibrium. Gas atoms act as trapping sites for vacancies and simultaneously represent the nucleation sites for bubbles.[33] Thus, a slight disturbance, such as defect concentration gradient, which comes from the stochastic functions ξ, can promote He bubble nucleation. Therefore, the number density of bubbles is large with high c_g. This also explained the presence of more bubbles in pure Ni than those in Ni/Gr. The late nucleation time will cause an increase in the overall c_g, corresponding to high free energy. Hence, the number and size of bubbles are large, thereby resulting in

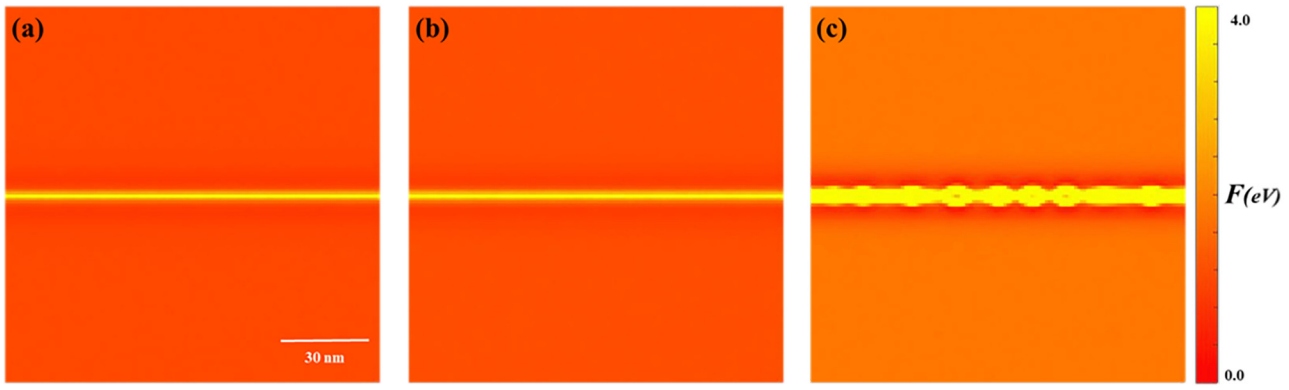

FIG. 8. Plot of the free energy at each grid with different P_g^0 values: (a) $P_g^0 = 2.5 \times 10^{-6}\tau^{-1}$, (b) $P_g^0 = 5 \times 10^{-6}\tau^{-1}$, and (c) $P_g^0 = 2.5 \times 10^{-5}\tau^{-1}$ when simulation time was 1200 τ.

Published under license by AIP Publishing.

considerable radiation-induced swelling and embrittlement in pure Ni. In Fig. 7(b), the bubble size increased more significantly with the rate of vacancy increased. As mentioned above, vacancies dominate the size change of the bubble.

IV. CONCLUSION

A phase-field model was proposed to investigate the He bubble evolution of the Ni/Gr nanocomposite in this work. The time evolution of the vacancy and He atoms concentration c_v, c_g, and the order parameter η were selected to describe the He bubble growth. First, several preliminary simulations were performed on the Ni system, which proved the feasibility of the phase-field model on the He growth problem. Afterward, simulations on the He bubble evolution of the Ni/Gr during constant irradiation were carried out. The results showed that Ni/Gr presented an earlier bubble nucleation time than pure Ni but formed bubbles of smaller size and lower quantity density eventually. Based on the image of bubble evolution in Ni/Gr, we can observe that the bubbles nucleated along the Ni/Gr interfaces preferentially, and the He depletion zone formed in the nearby interfaces, which confirmed that Ni/Gr interfaces inhibit He bubble growth. Combining the knowledge of bubble growth mechanisms, the results demonstrated that the number of irradiation-induced vacancies acted as an effective rate-controlling factor that determined the rate of bubble growth with respect to the He atoms. The higher bubble number in pure Ni than that in Ni/Gr was explained in terms of free energy. Finally, the simulation results and analysis may provide a reference for the design of the structural materials for Gen-IV nuclear reactors.

SUPPLEMENTARY MATERIAL

See the supplementary material for the calculation of interfacial energy between the solid and the bubble phase.

ACKNOWLEDGMENTS

This work was supported by the National Natural Science Foundation of China (NNSFC) (Grant No. 11705087), the Natural Science Foundation of Jiangsu Province (Grant No. BK20170776), and the Fundamental Research Funds for the Central Universities (Grant No. 56XAC18094).

REFERENCES

[1]M. Terrones, A. R. Botello-Méndez, J. Campos-Delgado, F. López-Urías, Y. I. Vega-Cantú, F. J. Rodríguez-Macías, A. L. Elías, E. Muñoz-Sandoval, A. G. Cano-Márquez, and J.-C. Charlier, Nano Today **5**, 351 (2010).
[2]J. Hwang, T. Yoon, S. H. Jin, J. Lee, T. S. Kim, S. H. Hong, and S. Jeon, Adv. Mater. **25**, 6724 (2013).
[3]T. L. Yang, L. Yang, H. Liu, H. L. Zhou, S. M. Peng, X. S. Zhou, F. Gao, and X. T. Zu, J. Alloys Compd. **692**, 49 (2017).
[4]R. I. González, F. Valencia, J. Mella, A. C. T. van Duin, K. P. So, J. Li, M. Kiwi, and E. M. Bringa, Appl. Phys. Lett. **109**, 033108 (2016).
[5]Y. Kim, J. Baek, S. Kim, S. Kim, S. Ryu, S. Jeon, and S. M. Han, Sci. Rep. **6**, 24785 (2016).
[6]K. L. Murty and I. Charit, J. Nucl. Mater. **383**, 189 (2008).
[7]P. Yvon and F. Carré, J. Nucl. Mater. **385**, 217 (2009).
[8]R. W. Grimes, R. J. Konings, and L. Edwards, Nat. Mater. **7**, 683 (2008).
[9]H. McCoy, Jr., "Status of materials development for molten salt reactors," Report No. ORNL/TM-5920, 1978.
[10]H. Ullmaier, Nucl. Fusion **24**, 1039 (1984).
[11]H. Huang, X. Tang, F. Chen, J. Liu, X. Sun, and L. Ji, J. Nucl. Mater. **510**, 1 (2018).
[12]Y. Li, S. Hu, X. Sun, and M. Stan, npj Comput. Mater. **3**(1), 16 (2017).
[13]P. C. Millett and M. Tonks, Comput. Mater. Sci. **50**, 2044 (2011).
[14]M. R. Tonks, A. Cheniour, and L. Aagesen, Comput. Mater. Sci. **147**, 353 (2018).
[15]K. Ahmed, J. Pakarinen, T. Allen, and A. El-Azab, J. Nucl. Mater. **446**, 90 (2014).
[16]X. Ma, S. Shi, C. Woo, and L. Chen, Comput. Mater. Sci. **23**, 283 (2002).
[17]K. Chang, G.-G. Lee, and J. Kwon, Radiat. Eff. Defects Solids **171**, 242 (2016).
[18]N. Moelans, B. Blanpain, and P. Wollants, Calphad **32**, 268 (2008).
[19]C. Lu, L. Niu, N. Chen, K. Jin, T. Yang, P. Xiu, Y. Zhang, F. Gao, H. Bei, S. Shi, M. R. He, I. M. Robertson, W. J. Weber, and L. Wang, Nat. Commun. **7**, 13564 (2016).
[20]J. W. Cahn and J. E. Hilliard, J. Chem. Phys. **28**, 258 (1958).
[21]S. M. Allen and J. W. Cahn, Acta Metall. **27**, 1085 (1979).
[22]P. C. Millett, A. El-Azab, S. Rokkam, M. Tonks, and D. Wolf, Comput. Mater. Sci. **50**, 949 (2011).
[23]L.-Q. Chen and W. Yang, Phys. Rev. B **50**, 15752 (1994).
[24]H. Huang, X. Tang, F. Chen, F. Gao, Q. Peng, L. Ji, and X. Sun, J. Alloys Compd. **765**, 253 (2018).
[25]C.-C. Hu, T.-N. Yang, H.-B. Huang, J.-M. Hu, J.-J. Wang, Y.-G. Shi, D.-N. Shi, and L.-Q. Chen, Appl. Phys. Lett. **108**, 141908 (2016).
[26]V. Chernikov, H. Trinkaus, P. Jung, H. J. Bierfeld, J. V. Lakhotkin, and H. Ullmaier, J. Nucl. Mater. **170**, 31 (1990).
[27]H. Trinkaus, Radiat. Eff. **78**, 189 (2006).
[28]H. Trinkaus and B. N. Singh, J. Nucl. Mater. **323**, 229 (2003).
[29]C. Wang, C. Ren, W. Zhang, H. Gong, P. Huai, Z. Zhu, H. Deng, and W. Hu, Comput. Mater. Sci. **107**, 54 (2015).
[30]F. Gao, H. L. Heinisch, and R. J. Kurtz, J. Nucl. Mater. **386–388**, 390 (2009).
[31]I. Zacharie, S. Lansiart, P. Combette, M. Trotabas, M. Coster, and M. Groos, J. Nucl. Mater. **255**, 85 (1998).
[32]A. J. Markworth, Metall. Trans. **4**, 2651 (1973).
[33]P. C. Millett, A. El-Azab, and D. Wolf, Comput. Mater. Sci. **50**, 960 (2011).

Published under license by AIP Publishing.